University of Sistan and Baluchestan

Challenges in Nano and Micro Scale Science and Technology

Online ISSN: 2821 - 000X

Effect of Cadmium on Structure, Corrosion, and Magnetic Properties of Polymer–Spinel Ferrite Composite Coatings Deposited by EPD

Morteza Khosravi[1]✉ | Shahriar Sharafi[2] | Ahmad Irannejad[2]

1. Department of Materials Engineering, Faculty of Engineering, University of Sistan and Baluchestan, Zahedan, Iran.
2. Department of Materials Engineering and Metallurgy, Faculty of Engineering, Shahid Bahonar University of Kerman, Kerman, Iran.

Corresponding Author's Email: mkhosravi@eng.usb.ac.ir

Article Info

Article type:
Research Article

Article history:
Received: 10 April 2026
Received in revised form: 24 April 2026
Accepted: 28 April 2026
Published Online: 06 May 2026

Keywords:
High-entropy spinel ferrite,
Electrophoretic deposition,
Corrosion resistance,
Magnetic properties

ABSTRACT

High-entropy spinel ferrites (HESFs) have emerged as promising multifunctional materials due to their tunable magnetic and corrosion properties. In this study, composite coatings composed of six high-entropy spinel ferrite compositions and polyethyleneimine (PEI) were deposited on copper substrates via electrophoretic deposition (EPD). The effects of Cd incorporation and polymerization time (15 and 30 h at 180 °C) on microstructure, magnetic behavior, and corrosion performance were systematically investigated. Zeta potential values shifted from near-neutral (+1.57 to −0.94 mV) to more negative values (−6.81 to −10.46 mV) after 3 min under an electric field, indicating improved electrophoretic mobility. Uniform coatings were obtained under optimized conditions (200 V, 3 min, 2 g/L SDS). Increasing polymerization time enhanced coating cohesion but promoted crack growth, especially in Cd-containing samples.All coatings exhibited ferromagnetic behavior, although magnetic parameters decreased compared to powders due to polymer-induced dilution and reduced interparticle interactions. Electrochemical results showed that Cd incorporation reduced corrosion current density from 2.15 μA/cm² to as low as 0.1–0.5 μA/cm², indicating improved corrosion resistance. However, increasing polymerization time could increase icorr (e.g., from 0.1 to 5 μA/cm²) due to crack propagation. EIS analysis revealed a maximum total resistance of ~7544 Ω·cm², confirming enhanced corrosion protection under optimal conditions. Overall, coating performance is governed by the interplay between composition, polymerization, and microstructure, and optimal conditions are essential for achieving high-performance multifunctional coatings.

1. INTRODUCTION

The concept of high-entropy materials originated in the early 2000s with high-entropy alloys and was later extended to oxide systems, leading to the development of high-entropy oxides (HEOs)[1]. While early studies mainly focused on powder synthesis and fundamental properties, recent research has shifted toward functional applications. However, high-entropy ferrite coatings, particularly those prepared by electrophoretic deposition and their corrosion behavior, remain insufficiently explored[2].

High-entropy materials have emerged as a new paradigm in materials science since the introduction of the high-entropy alloy concept, where multiple principal elements are incorporated in near-equiatomic compositions to form stable solid solutions[3]. The extension of this concept to oxide systems has led to the development of high-entropy oxides (HEOs), which exhibit remarkable structural stability and unique functional properties due to their high configurational entropy and severe lattice distortion [4]. In these materials, the random distribution of multiple cations within a single crystallographic lattice can significantly modify physical and chemical properties, including electrical conductivity, catalytic activity, magnetic behavior, and corrosion resistance[5-9].

Among different families of high-entropy oxides, high-entropy spinel ferrites (HESFs) have attracted increasing attention because of their multifunctional properties and structural versatility[10]. Spinel ferrites generally possess the formula MFe_2O_4, where M represents a divalent metal cation occupying tetrahedral (A) or octahedral (B) sites within the cubic spinel structure. The magnetic properties

How to Cite this paper: Khosravi M. Sharafi Sh. Irannejad A. Effect of Cadmium on Structure, Corrosion, and Magnetic Properties of Polymer–Spinel Ferrite Composite Coatings Deposited by EPD. *Challenges in Nano and Micro Scale Science and Technology*. 2026; 14(2): 1-15. DOI: 10.22111/cnmst.2026.55051.1292

DOI: 10.22111/cnmst.2026.55051.1292

of spinel ferrites originate from superexchange interactions between cations located in these crystallographic sites, which strongly depend on the chemical composition and cation distribution [11]. Incorporating multiple transition-metal ions such as Mn, Co, Ni, Zn, Cu, and Cd into the spinel lattice leads to complex cation arrangements and enhanced configurational entropy, which can significantly influence magnetic interactions, lattice distortion, and electron hopping mechanisms. As a result, high-entropy spinel ferrites may exhibit tunable magnetic properties, improved thermal stability, and enhanced functional performance compared with conventional ferrites [12].

In recent years, several studies have focused on the synthesis and characterization of high-entropy spinel ferrites for applications in electromagnetic wave absorption, catalysis, energy storage, and magnetic devices[13-19]. The presence of multiple transition metals with different ionic radii and valence states can generate strong lattice distortion and modify magnetic exchange interactions, which in turn affect the saturation magnetization, coercivity, and magnetic anisotropy of the material [20, 21]. These characteristics make high-entropy ferrites promising candidates for advanced multifunctional materials[22].

In addition to bulk properties, the development of functional ferrite coatings on metallic substrates has attracted considerable attention in corrosion protection and multifunctional surface engineering [23]. Ferrite-based coatings can serve as protective barriers that limit the diffusion of corrosive species and improve the durability of metallic substrates in aggressive environments such as chloride-containing solutions [24]. Furthermore, magnetic ferrite coatings may provide additional functionalities including electromagnetic shielding and catalytic activity [25]. Therefore, combining the high-entropy concept with ferrite coatings offers a promising strategy for designing advanced multifunctional protective materials.

Among various coating techniques, electrophoretic deposition (EPD) is considered one of the most versatile and cost-effective methods for producing ceramic and composite coatings[26]. EPD involves the migration of charged particles suspended in a liquid medium under the influence of an electric field, resulting in the formation of a uniform coating on a conductive substrate [27]. This technique offers several advantages including simple equipment, room-temperature processing, good control of coating thickness, and the ability to deposit complex ceramic materials on substrates with different shapes [28]. In addition, the incorporation of polymeric binders and surfactants into the suspension can significantly improve suspension stability, particle dispersion, and adhesion of the deposited coating [29].

Despite the growing interest in high-entropy spinel ferrites, most previous studies have primarily focused on powder synthesis and bulk magnetic characterization, while relatively limited research has been devoted to the fabrication of high-entropy ferrite coatings and the evaluation of their corrosion behavior on metallic substrates. Furthermore, systematic investigations comparing multiple compositional variations of high-entropy spinel ferrites within coating systems remain scarce in the literature. In particular, the influence of replacing individual cations within the high-entropy spinel lattice on the structural characteristics, magnetic properties, and corrosion performance of electrophoretically deposited coatings has not been comprehensively studied.

Therefore, the present work aims to investigate the structural characteristics, magnetic properties, and corrosion behavior of six high-entropy spinel ferrite coatings deposited on copper substrates. Six compositions including (Mn,Co,Ni,Zn,Cu) Fe_2O_4, (Mn,Co,Ni,Zn,Cd) Fe_2O_4, (Mn,Co,Ni,Cd,Cu) Fe_2O_4, (Mn,Co,Cd,Zn,Cu) Fe_2O_4, (Mn,Cd,Ni,Zn,Cu) Fe_2O_4 and (Cd,Co,Ni,Zn,Cu) Fe_2O_4 were prepared and subsequently deposited onto copper substrates via the electrophoretic deposition technique. The EPD suspension consisted of high-entropy spinel ferrite powder, polyethyleneimine (PEI), sodium dodecyl sulfate (SDS), and an active copper anode, resulting in the formation of a polymer-matrix composite coating.

The novelty of this study lies in the systematic comparison of six compositional variations of high-entropy spinel ferrites in electrophoretically deposited coatings and the investigation of their combined structural, magnetic, and corrosion properties. In addition, this work introduces the use of an active copper anode during the EPD process, which promotes in situ generation of Cu^{2+} ions and enhances coating adhesion and formation through complexation with the polymer matrix. Another key innovation is the development of a polymer-based composite coating incorporating magnetic spinel ferrite particles, enabling the integration of protective and magnetic functionalities within a single coating system. This approach provides new insights into the role of cation substitution in high-entropy spinel systems, highlights the significance of process chemistry in EPD, and demonstrates the potential of electrophoretically deposited high-entropy ferrite/polymer composite coatings as multifunctional protective layers for metallic substrates.

2. EXPERIMENTAL

2.1. Materials and Equipment

Spinel ferrite powders synthesized via solution combustion synthesis (SCS) were used as the coating material; detailed synthesis procedures have been comprehensively described in previous studies [30].

Particle size reduction and homogenization were performed using a ball mill operating at a controlled speed of 100 rpm. Isopropanol (IPA) was used as the suspension medium. Polyethyleneimine (PEI, 1 g/L) served as a charging and binding agent, while sodium dodecyl sulfate (SDS) was added as a surfactant at concentrations of 1 and 2 g/L to prepare two distinct suspensions.

Electrophoretic deposition (EPD) was carried out using a DC power supply capable of delivering up to 300 V. A glass electrophoretic cell with a fixed inter-electrode distance of 1 cm was employed. Both electrodes were made of copper, with cathodes of 10×10 mm and anodes

of 30×30 mm dimensions. A precision balance with an accuracy of 0.0001 g was used to determine the deposited mass. A drying oven was utilized for post-deposition drying and polymerization.

2.2. Electrophoretic Deposition Process

Pure copper substrates were used as both cathode (10×10 mm) and anode (30×30 mm). The substrates were mechanically polished using silicon carbide abrasive papers with grit sizes of 400, 1000, and 1500 to obtain a smooth and uniform surface. Subsequently, the samples were ultrasonically cleaned in acetone and dried with hot air to remove any surface contaminants. The same preparation procedure was applied to both electrodes.

The as-synthesized spinel ferrite powders were ball-milled for 2 h at 100 rpm to achieve uniform particle size distribution. Suspensions were prepared by dispersing 1 g/L of the powder in isopropanol. PEI (1 g/L) was added to enhance particle charging and suspension stability. SDS was introduced at two different concentrations (1 and 2 g/L), resulting in two separate suspensions.

The suspensions were then subjected to probe ultrasonication for 10 min to ensure complete dispersion and to prevent particle agglomeration.

EPD was conducted in a glass cell with a fixed electrode spacing of 1 cm (Fig.1). Both electrodes were made of copper. The use of a copper anode was found to be critical, as Cu^{2+} ions released during the process played a significant role in promoting deposition and improving coating adhesion. In contrast, replacing the anode with stainless steel resulted in poor deposition quality and non-uniform coatings.

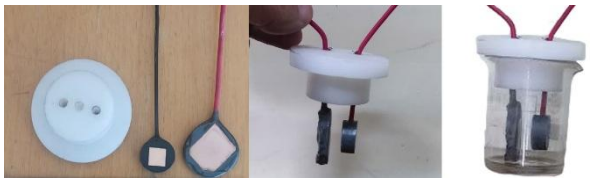

Fig. 1. Components of an electrophoretic coating cell and electrode placement

Deposition experiments were performed at applied voltages of 150, 200, and 250 V. Among these, 200 V provided the best combination of coating uniformity and adhesion and was therefore selected for subsequent experiments. After deposition, the mass of the deposited coatings was measured using a high-precision balance.

2.3. Drying and Polymerization

After deposition, the coated samples were air-dried at room temperature for 24 h. Subsequently, polymerization of PEI was carried out in a drying oven at 180 °C. Two different polymerization times (15 and 30 h) were investigated to evaluate their effect on coating strength and adhesion.

2.4. Characterization Techniques

The morphology and microstructure of both powders and coatings were examined using FESEM (KYKY EM8000F). Images at various magnifications provided insight into particle distribution, coating uniformity, and adhesion. Elemental composition and distribution were analyzed using energy-dispersive X-ray spectroscopy (EDS) and elemental mapping.

Magnetic properties of the powders and coatings were measured using a vibrating sample magnetometer (Meghnatis Daghigh Kavir) at room temperature. Hysteresis loops were recorded in a magnetic field range of −14 to +14 kOe. Parameters including saturation magnetization (Ms), remanent magnetization (Mr), and coercivity (Hc) were extracted.

Corrosion resistance and electrochemical behavior of the coatings were evaluated using an EG&G system (Model 1025) in a 3.5 wt.% NaCl solution at room temperature. A three-electrode configuration was used, consisting of the coated sample as the working electrode, an Ag/AgCl reference electrode, and a platinum counter electrode.

An AC perturbation of 10 mV was applied over a frequency range from 0.1 Hz to 100 kHz. Nyquist and Bode plots were obtained, and equivalent circuit modeling was performed using ZsimpWin software to extract parameters such as charge transfer resistance (R_{ct}), double-layer capacitance (C_{dl}), and coating resistance (R_f).

Potentiodynamic polarization tests were conducted in the same electrolyte and cell configuration as EIS using an Autolab system (Model: PGSTAT302N). The potential was scanned from −500 to +1500 mV vs. Ag/AgCl at a scan rate of 1 $mV \cdot s^{-1}$. Corrosion parameters, including corrosion potential (E_{corr}) and corrosion current density (i_{corr}), were determined from the polarization curves.

The stability of the suspensions was evaluated by measuring the zeta potential using a NanoPlus Zeta Nanoparticle Analyzer (Class 1 Laser). High absolute values of zeta potential indicate better suspension stability and reduced particle agglomeration.

3. RESULTS AND DISCUSSION

3.1. Zeta Potential Evolution and EPD Mechanism

The zeta potential results (Table .1) show that the suspensions initially possess near-neutral values (+1.57 mV for 1 g/L SDS and −0.94 mV for 2 g/L SDS), indicating weak electrostatic stabilization and insufficient intrinsic electrophoretic mobility of ferrite particles. After 3 min under an electric field, the zeta potential shifts to more negative values (−6.81 and −10.46 mV, respectively), reflecting the migration and depletion of positively charged species toward the cathode and enrichment of the suspension with anionic species (mainly SDS). The increase in the absolute zeta potential with SDS concentration confirms its active role in regulating charge balance and the electrical double layer during deposition.

Table 1
Results of zeta potential measurements for different suspensions

Sample Name	Powder concentration (g/L)	PEI concentration (g/L)	SDS concentration (g/L)	Time spent in cell (min)	Zeta potential (mV)
$I_1S_1T_0$	1	1	1	0	1.57
$I_1S_1T_3$	1	1	1	3	-6.81
$I_1S_2T_0$	1	1	2	0	-0.94
$I_1S_2T_3$	1	1	2	3	-10.46

PEI adsorbs on ferrite particles and introduces localized positive charges [31], but alone cannot ensure effective mobility. In contrast, SDS forms electrostatic PEI–SDS complexes [32, 33] and modifies the particle double layer [34], resulting in a conditionally stable suspension responsive to the electric field [35]. The absence of deposition without SDS highlights its essential role beyond simple stabilization.

Coating formation occurs only with a copper anode, which releases Cu^{2+} ions in situ under 200 V. These ions form PEI–Cu^{2+} complexes with enhanced positive charge [36] and act as ionic bridges between particles and polymer chains, improving aggregation and adhesion [37]. EDS mapping confirms the co-deposition of copper and ferrite, while control experiments with non-copper anodes or direct salt addition yield poor coatings, emphasizing the importance of in situ Cu^{2+} generation.

Thus, the process is best described as cathodic EPD assisted by an active anode. SDS enables dispersion and electrostatic interactions, PEI serves as a carrier and complexing agent, and Cu^{2+} ions generate positively charged complexes that migrate toward the cathode and co-deposit as a ferrite–polymer–copper composite [38-40]. The dependence on SDS, zeta potential evolution, and the necessity of a copper anode indicate a multi-component, reaction-driven mechanism rather than classical EPD. This synergistic interaction leads to selective cathodic deposition, improved adhesion, and enhanced coating integrity, highlighting the importance of optimizing both suspension chemistry and electrochemical conditions.

3.2. Effect of Deposition Parameters on Coating Formation

The electrophoretic deposition (EPD) behavior of high-entropy spinel ferrite ((Mn,Co,Ni,Cu,Zn) Fe_2O_4) coatings on copper substrates was systematically investigated by varying the applied voltage (150–250 V), deposition time (1–3 min), and SDS concentration (1 and 2 g/L). The deposited mass per unit area and surface morphology were employed as quantitative and qualitative criteria for evaluating coating performance.

The results (Figs. 2 and 3) demonstrate that increasing the deposition time from 1 to 3 min leads to a monotonic increase in deposited mass across all applied voltages, in agreement with classical EPD theory, where prolonged electric field exposure enhances the migration of charged species toward the cathode [41-43]. Furthermore, the deposition rate is strongly dependent on the applied voltage, with higher voltages generating greater electrophoretic driving forces and, consequently, steeper mass accumulation [44].

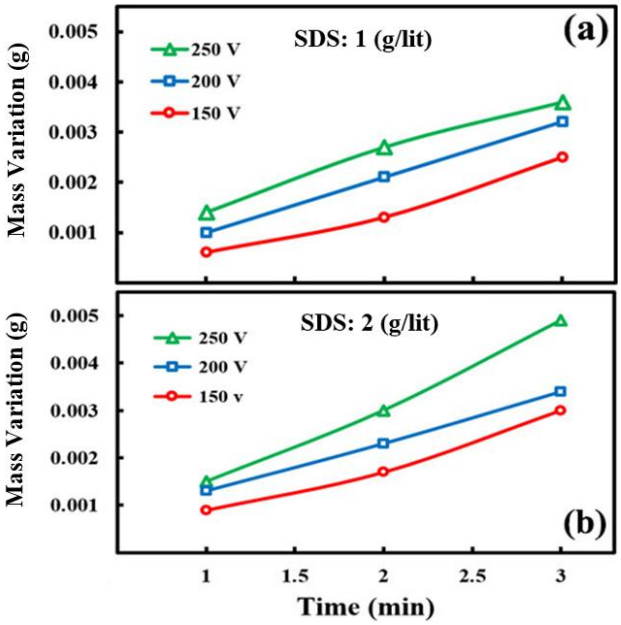

Fig. 2. Changes in settlement mass over time for different SDS contents

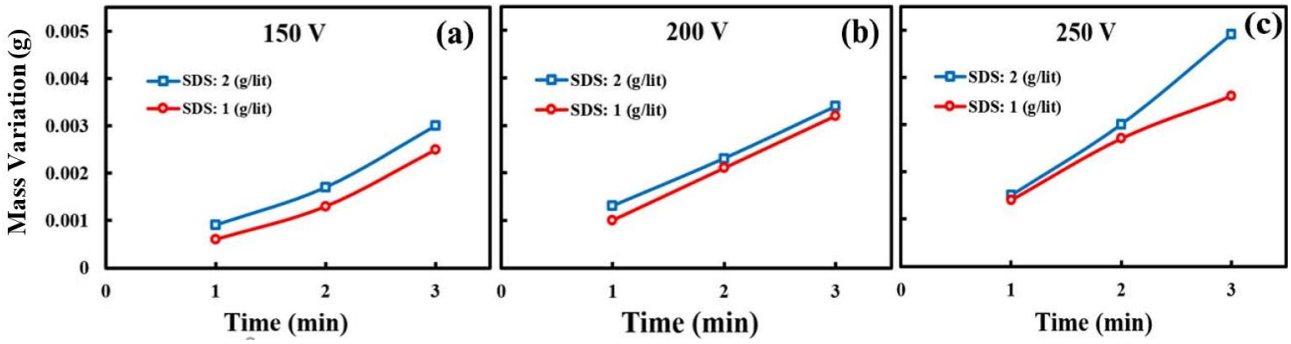

Fig. 3. Changes in settlement mass over time for different potentials

At a constant deposition time (Fig. 4), increasing the voltage from 150 to 250 V significantly increases the deposited mass. However, deposition at 250 V, although rapid, results in coating inhomogeneity, internal stresses, and the formation of microcracks due to excessive deposition rates [27]. In contrast, coatings obtained at 150 V exhibit superior uniformity but insufficient thickness and, in some cases, incomplete substrate coverage. Therefore, 200 V represents an optimal intermediate condition, providing a balanced trade-off between deposition kinetics and coating integrity.

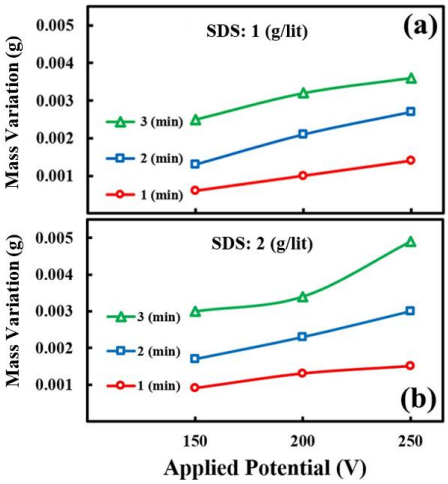

Fig. 4. Changes in settlement mass over potential for for different SDS contents

The influence of SDS concentration is equally significant. Increasing SDS from 1 to 2 g/L enhances the deposited mass under all investigated conditions (Figures 2 to 4) [45, 46], which can be attributed to improved particle dispersion, reduced agglomeration, and enhanced suspension stability [47, 48]. Moreover, SDS plays a crucial role in regulating electrostatic interactions among PEI, Cu^{2+} ions, and ferrite particles [32], thereby facilitating the formation of stable, charged complexes with improved electrophoretic mobility [49]. This results in more uniform and controlled deposition.

It is important to note that maximum deposited mass does not necessarily correspond to optimal coating quality. At excessively high deposition rates, particles lack sufficient time to rearrange and densify, leading to structural defects and reduced coating integrity [41, 50]. In contrast, the condition of 200 V, 3 min, and 2 g/L SDS provides a controlled deposition regime that enables homogeneous particle distribution, complete surface coverage, and the formation of dense, crack-free coatings with relatively uniform thickness, as confirmed by optical observations (Fig.5).

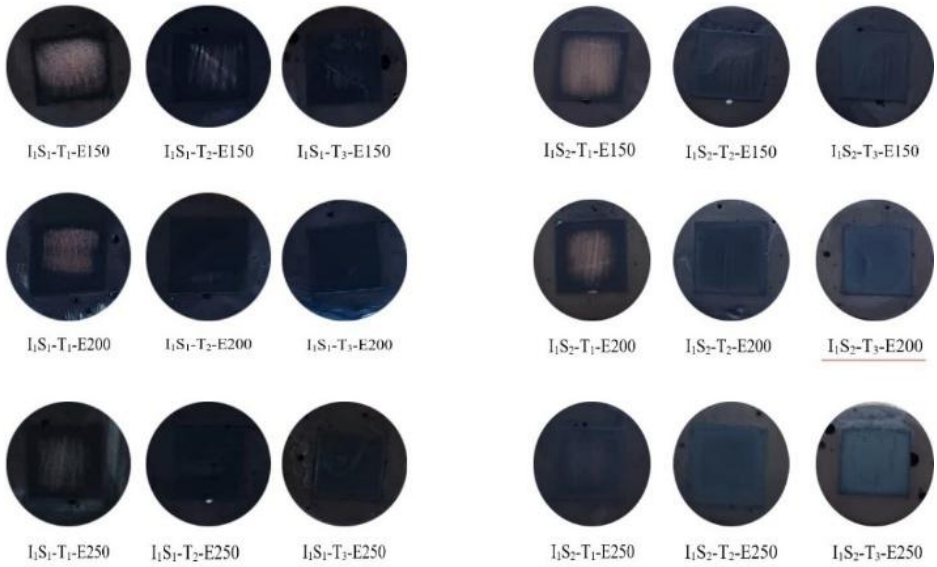

Fig. 5. Optical image of the surface of coated samples under different coating conditions

3.3. Microstructural Evolution and Cracking Behavior of EPD Coatings

Under optimized EPD conditions (200 V, 3 min), uniform and relatively adherent composite coatings composed of high-entropy spinel ferrite particles and polyethyleneimine (PEI) were successfully deposited on copper substrates. The use of a non-aqueous propanol medium improved suspension stability and suppressed undesirable side reactions, enabling controlled coating formation [51, 52]. Post-deposition thermal polymerization at 180 °C for 15 and 30 h was applied to evaluate its effect on microstructure and coating integrity.

SEM observations (Fig. 6) show that increasing the polymerization time from 15 to 30 h results in significantly larger surface cracks in all coatings. However, the severity

of cracking is strongly dependent on the ferrite composition, with the following trend: (Mn,Co,Ni,Cu,Zn) Fe_2O_4 < (Mn,Cd,Ni,Cu,Zn) Fe_2O_4 < (Mn,Co,Cd,Cu,Zn) Fe_2O_4 < (Mn,Co,Ni,Cd,Zn) Fe_2O_4 < (Cd,Co,Ni,Cu,Zn) Fe_2O_4 < (Mn,Co,Ni,Cu,Cd) Fe_2O_4. This indicates that, although prolonged polymerization promotes crack growth, the presence and role of Cd are decisive in intensifying this behavior.

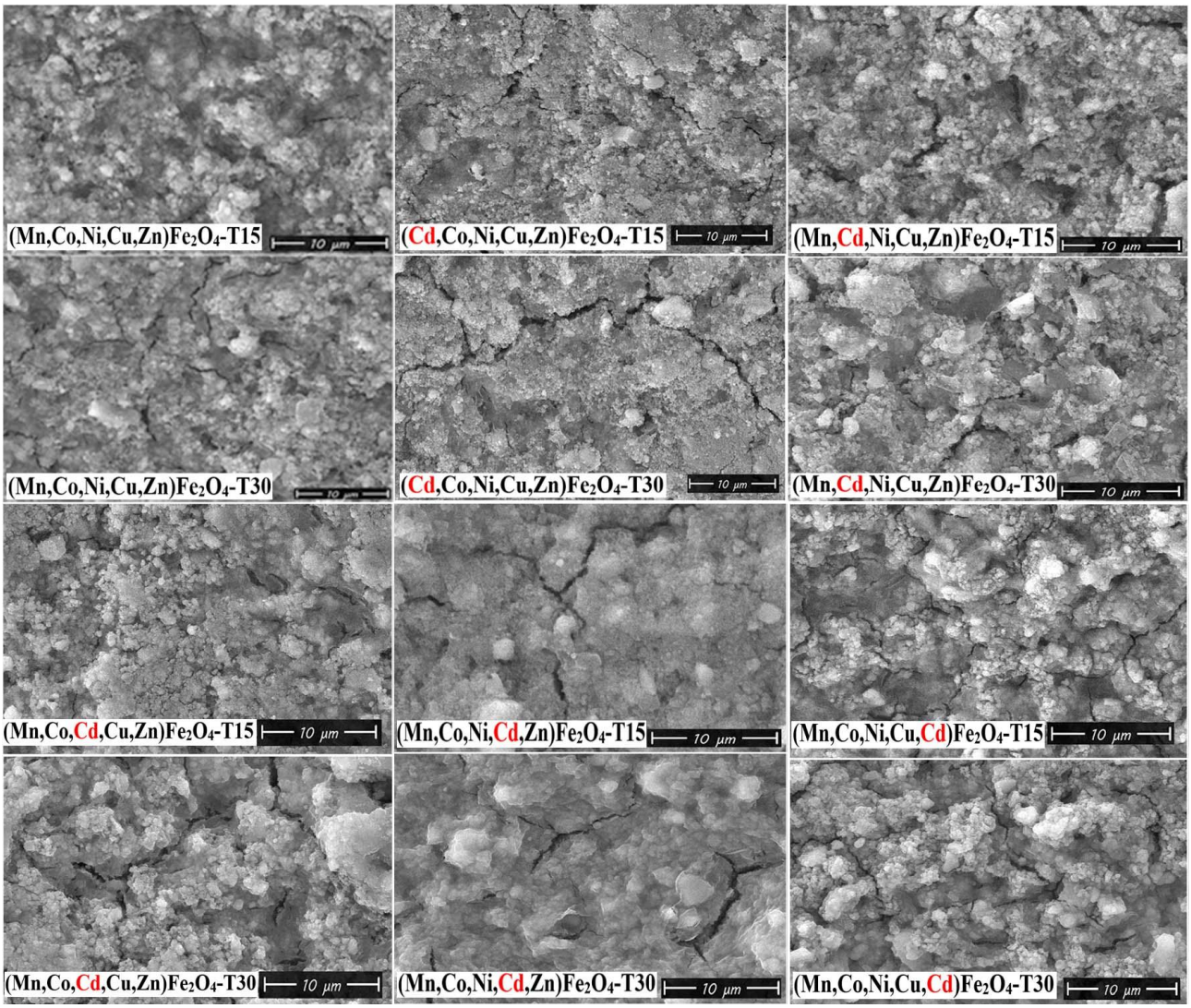

Fig. 6. SEM images of the coating surface of different ferrite spinel samples (T15: polymerized for 15 hours at 180 °C and T30: polymerized for 30 hours at 180 °C).

Mechanistically, longer polymerization enhances PEI crosslinking, reduces molecular mobility, and increases stiffness and elastic modulus [53, 54]. This leads to greater volumetric shrinkage during curing and restricts uniform stress relaxation in constrained coatings on metallic substrates [55-57]. Consequently, residual stresses are mainly released through crack propagation and widening rather than new crack nucleation [58].

Cross-sectional SEM (Fig.7) confirms the formation of a continuous coating layer with good interfacial contact after 30 h. Elemental mapping and EDS results (Fig.8 , Table.2) reveal a homogeneous distribution of Fe, Mn, Co, Ni, Cu, Zn, and Cd, consistent with the nominal compositions, indicating that the EPD process preserves chemical uniformity.

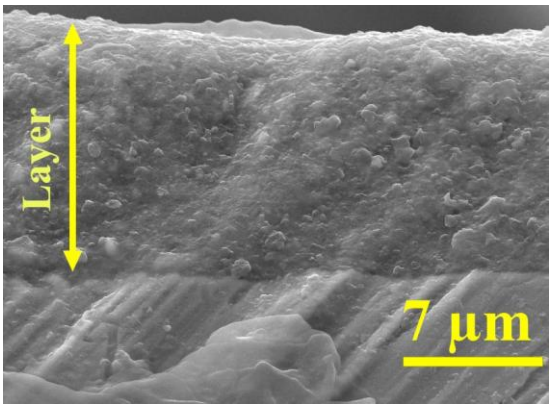

Fig. 7. Scanning electron microscope image of the cross-section of the (Mn,Co,Ni,Cu,Zn)Fe_2O_4 coating on a copper substrate

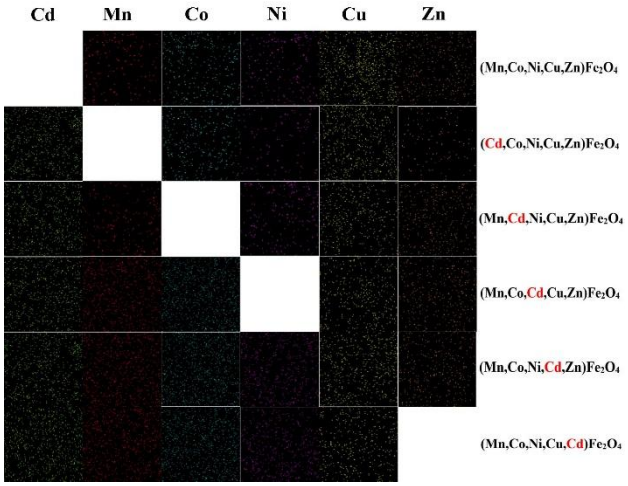

Fig. 8. EDS-mapping of samples coated with different spinel ferrite powders

Despite larger cracks, coatings polymerized for 30 h exhibit superior adhesion and mechanical stability [59, 60]. Enhanced polymer network formation increases interfacial bonding density, reduces soluble fractions, and improves mechanical interlocking [61, 62]. As a result, these coatings show higher resistance to water exposure and manual abrasion without macroscopic delamination, indicating that larger crack size reflects a shift in stress-relief mechanisms rather than reduced integrity.

Table 2
Chemical composition (EDS) of the surface of samples coated with different spinel ferrite powders

sample	Fe	Mn	Co	Ni	Cu	Zn	Cd
(Mn,Co,Ni,Cu,Zn)Fe_2O_4	55.93	4	4.64	5.26	24.22	5.95	-
(Cd,Co,Ni,Cu,Zn)Fe_2O_4	52.1	-	6.53	5.72	25.96	5.08	4.61
(Mn,Cd,Ni,Cu,Zn)Fe_2O_4	52.94	5.11	-	4.93	26.11	5.83	5.08
(Mn,Co,Cd,Cu,Zn)Fe_2O_4	50.78	4.83	4.73	-	27.56	5.90	6.20
(Mn,Co,Ni,Cd,Zn)Fe_2O_4	51.92	5.48	6.81	5.92	20.17	4.46	5.24
(Mn,Co,Ni,Cu,Cd)Fe_2O_4	56.27	4.58	5.15	5.30	24.53	-	4.17

The ferrite composition, particularly Cd incorporation, significantly influences cracking behavior. Due to its larger ionic radius and preferential octahedral occupancy, Cd induces lattice distortion and alters particle surface energy [63-65], reducing compatibility with the PEI matrix and increasing interfacial stress concentration. Consequently, Cd-containing coatings exhibit more pronounced crack growth during extended polymerization, consistent with experimental observations.

3.4. Magnetic Properties of EPD Coatings

The magnetic properties of the electrophoretically deposited (EPD) coatings were evaluated using vibrating sample magnetometry (VSM). The hysteresis loops (Fig.9) and the extracted parameters, including saturation magnetization (M_s), remanent magnetization (M_r), and coercivity (H_c) (Fig.10), reveal that all ferrite-based coatings exhibit lower magnetic parameters compared to their corresponding powders. For example, the saturation magnetization (M_s), remanent magnetization (M_r), and coercivity (H_c) of the (Cd,Co,Ni,Cu,Zn)Fe_2O_4 powder are 72 emu/g, 23 emu/g, and 138 Oe, respectively, whereas the corresponding values for the coating prepared from the same powder are 84 emu/g, 14 emu/g, and 44 Oe, respectively [30]. This consistent reduction is in full agreement with previously reported behavior in magnetic polymer–ferrite composite systems and can be attributed to the combined effect of several physical and magnetic mechanisms [66].

The primary factor is the presence of polyethyleneimine (PEI) as a non-magnetic polymeric matrix. Due to the absence of intrinsic magnetic moments, PEI induces a magnetic dilution effect, reducing the overall magnetization per unit mass of the coating. Consequently, both Ms and Mr decrease relative to the pure ferrite powders, while the intrinsic ferromagnetic nature of the spinel ferrite phase is preserved. This phenomenon is widely reported in ferrite–polymer composites and is considered an inherent characteristic of such systems [67-69].

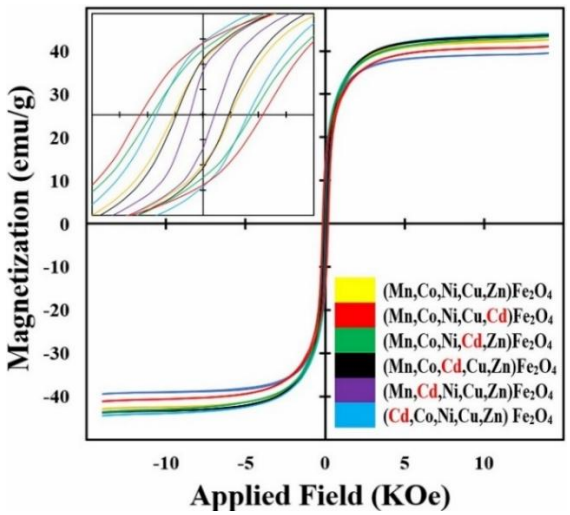

Fig. 9. Hysteresis curve of the coating of various spinel ferrite powders obtained from VSM test

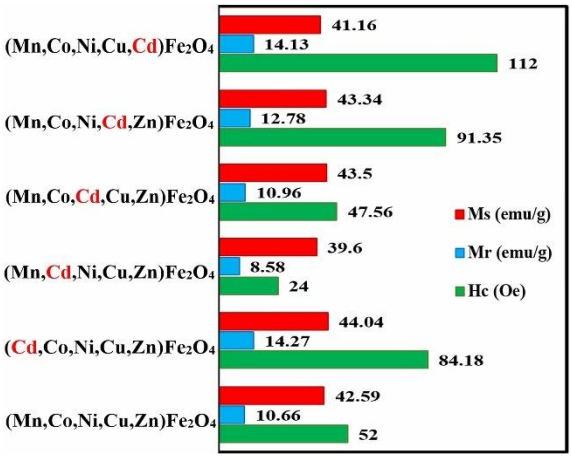

Fig. 10. Values of saturation magnetization (Ms), remanence magnetization (Mr) and coercivity (Hc) obtained from VSM test

A second contributing factor is the weakening of interparticle exchange interactions. In powder form, close contact between ferrite particles enhances exchange coupling and stabilizes magnetic domains. In contrast, the polymer layers in EPD coatings increase the effective interparticle distance, limiting spin exchange interactions. This leads to a reduction in both remanent magnetization and coercivity, as domain wall motion becomes easier and domain stability decreases [70-72].

Another important factor is the presence of metallic copper (Cu^0) within the coating structure. Based on EDS results, approximately 5 at.% Cu exists as a reduced metallic phase outside the spinel lattice. Metallic copper exhibits diamagnetic behavior, and its presence further weakens the overall magnetic response of the coating. In addition to reducing Ms and Mr, this non-magnetic phase decreases the effective magnetic anisotropy, resulting in lower coercivity. Similar behavior has been reported in multiphase systems containing ferrites and non-magnetic metals [73, 74].

Despite the reduction in magnetic parameters, all coatings exhibit well-defined ferromagnetic hysteresis loops, indicating that the spinel structure remains intact during EPD and subsequent polymerization. No transition to paramagnetic or superparamagnetic behavior is observed. The retention of ferromagnetic properties is significant for practical applications, enabling the use of these coatings in multifunctional systems such as smart coatings, electromagnetic wave absorbers, and protective coatings with magnetic responsiveness [75, 76].

Furthermore, the relative differences between the magnetic parameters of powders and coatings remain within a similar range across all compositions. This uniformity suggests that the EPD process ensures homogeneous particle distribution within the polymer matrix and prevents the formation of detrimental secondary phases [77, 78]. Overall, the results demonstrate that EPD enables the fabrication of uniform composite coatings with predictable and controllable magnetic properties.

3.5. Potentiodynamic Corrosion Behavior of EPD Coatings

The potentiodynamic polarization curves of the coatings prepared with polymerization times of 15 and 30 h in 3.5 wt.% NaCl at room temperature are shown in Fig.11. Prior immersion of samples for 2 h ensured partial equilibration with the corrosive environment and minimized transient effects associated with initial chloride adsorption and electrolyte penetration; thus, the extracted parameters represent relatively stable system behavior [79]. Tafel extrapolation was performed using NOVA software, and the corrosion current density (i_{corr}), corrosion potential (E_{corr}), and anodic and cathodic Tafel slopes (β_a, β_c) are reported in Table 4-7. Although the Stern–Geary relation was used to estimate polarization resistance, R_p values in cracked and heterogeneous coating systems are strongly influenced by cell geometry and localized activation; therefore, interpretation is primarily based on i_{corr} trends and relative comparisons [80, 81].

Comparison between the Cd-free coating ($(Mn,Co,Ni,Cu,Zn)Fe_2O_4$) and Cd-containing samples shows that Cd incorporation generally leads to a significant reduction in corrosion current density. The i_{corr} value decreases from 2.15 µA/cm² for the Cd-free sample (15 h) to values in the range of 0.1–1.12 µA/cm² for most Cd-containing coatings; for instance, $(Mn,Co,Cd,Cu,Zn)Fe_2O_4$-T15 and $(Cd,Co,Ni,Cu,Zn)Fe_2O_4$-T15 exhibit i_{corr} values of 0.1 and 0.225 µA/cm², respectively. This reduction indicates slower corrosion kinetics and enhanced corrosion resistance, which can be attributed to the role of Cd in modifying the electronic structure of the spinel phase and facilitating the formation of more stable and less permeable passive films. Due to its lower reduction potential relative to some transition cations, Cd can alter charge distribution and surface energy, promoting the formation of stable iron oxides with improved resistance to chloride penetration [51].

However, this beneficial effect depends strongly on coating microstructure and Cd distribution. For example, $(Mn,Co,Ni,Cu,Cd)Fe_2O_4$-T15 exhibits a relatively higher i_{corr} (0.2 µA/cm²), indicating that phase chemistry alone does not govern corrosion behavior. Microstructural observations show that crack size and connectivity increase in the order: $(Mn,Co,Ni,Cu,Zn)Fe_2O_4$ < (Mn,Cd,Ni,Cu,Zn) Fe_2O_4 < (Mn,Co,Cd,Cu,Zn) Fe_2O_4 < (Mn,Co,Ni,Cd,Zn) Fe_2O_4 < (Cd,Co,Ni,Cu,Zn) Fe_2O_4 < (Mn,Co,Ni,Cu,Cd) Fe_2O_4. Larger and more connected cracks provide preferential pathways for chloride ingress and localized current concentration, thereby increasing corrosion rates [52].

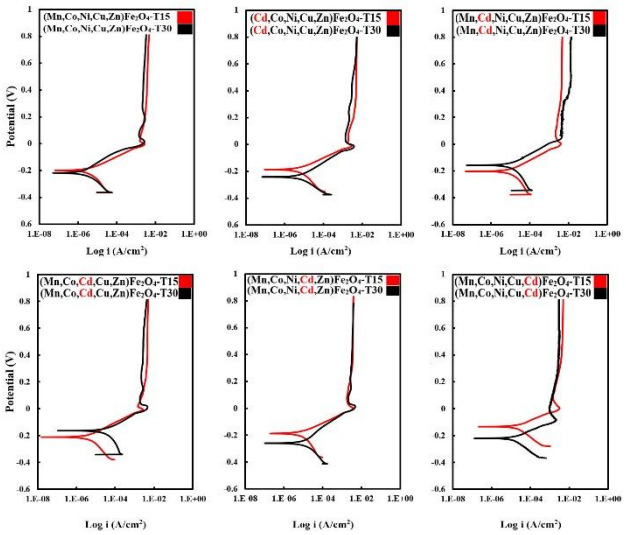

Fig. 11. Potentiodynamic polarization curves of coated samples with two polymerization times (T15: 15 hours and T30: 30 hours) in 3.5%Wt NaCl solution

Polymerization time also plays a critical role in corrosion behavior [82]. Increasing the time from 15 to 30 h enhances polymer network formation, reduces PEI solubility, and improves coating adhesion to the substrate [83], as confirmed by improved resistance to mechanical damage in aqueous environments. However, this is

accompanied by increased crack size due to curing shrinkage (Fig.6) [84]. This dual effect is reflected in polarization results: for instance, i_{corr} increases from 2.15 to 2.33 μA/cm² for (Mn,Co,Ni,Cu,Zn)Fe_2O_4 and dramatically from 0.1 to 5 μA/cm² for (Mn,Co,Cd,Cu,Zn)Fe_2O_4 upon increasing polymerization time. This indicates that crack growth can negate or even dominate the beneficial effects of improved adhesion.

In some cases, such as (Mn,Cd,Ni,Cu,Zn)Fe_2O_4, i_{corr} decreases from 0.5 to 0.35 μA/cm² with increasing polymerization time, reflecting competition between improved chemical integrity of the coating and crack-induced degradation. The dominance of each mechanism depends on ferrite composition and its interaction with the polymer matrix.

Table 3
Results of TOFEL extrapolation of potentiodynamic polarization curves

Sample	E_{corr} (V)	i_{corr} (μA/cm²)	βa (mV/dec)	βc (mV/dec)	Rp (Ω·cm²)
(Mn,Co,Ni,Cu,Zn)Fe_2O_4-T15	-0.1685	2.15	89	102	9,599
(Mn,Co,Ni,Cu,Zn)Fe_2O_4-T30	-0.1723	2.33	91	105	9,085
(Cd,Co,Ni,Cu,Zn)Fe_2O_4-T15	-0.187	0.225	50.3	62.1	53,600
(Cd,Co,Ni,Cu,Zn)Fe_2O_4-T30	-0.221	0.224	57.3	57.6	55,700
(Mn,Cd,Ni,Cu,Zn)Fe_2O_4-T15	-0.202	0.5	150	120	57,896
(Mn,Cd,Ni,Cu,Zn)Fe_2O_4-T30	-0.157	0.35	180	110	84,715
(Mn,Co,Cd,Cu,Zn)Fe_2O_4-T15	-0.21	0.1	60	120	170,000
(Mn,Co,Cd,Cu,Zn)Fe_2O_4-T30	-0.173	5	55	110	3,200
(Mn,Co,Ni,Cd,Zn)Fe_2O_4-T15	-0.188	1.12	89	152	14,850
(Mn,Co,Ni,Cd,Zn)Fe_2O_4-T30	-0.259	0.847	94	168	18,930
(Mn,Co,Ni,Cu,Cd)Fe_2O_4-T15	-0.133	0.2	120	95	28,500
(Mn,Co,Ni,Cu,Cd)Fe_2O_4-T30	-0.0003	0.12	85	65	42,000

Analysis of Tafel slopes provides further insight into electrochemical kinetics. For example, (Mn,Co,Ni,Cu,Zn)Fe_2O_4-T15 exhibits $\beta_a \approx 89$ mV/dec and $\beta_c \approx 102$ mV/dec, indicating relatively balanced anodic and cathodic contributions. In contrast, Cd-containing samples such as (Cd,Co,Ni,Cu,Zn)Fe_2O_4-T15 show lower β_a and β_c values (50.3 and 62.1 mV/dec), suggesting lower kinetic barriers; however, the simultaneous reduction in i_{corr} indicates that corrosion control is governed primarily by physical and chemical barrier effects rather than intrinsic reaction kinetics. Higher β values observed in compositions such as (Mn,Cd,Ni,Cu,Zn)Fe_2O_4 ($\beta_a \approx 150$–180 mV/dec, $\beta_c \approx 110$–120 mV/dec) indicate strong polarization and complex charge transfer pathways, consistent with reduced i_{corr} values [85].

The corrosion potential (E_{corr}) varies within a relatively narrow range (approximately −0.26 V to near 0 V). Although shifts toward more noble potentials, such as near 0 V for (Mn,Co,Ni,Cu,Cd)Fe_2O_4-T30, suggest reduced thermodynamic tendency for corrosion initiation, the presence of relatively high i_{corr} values in some cases indicates that E_{corr} alone is not a reliable indicator of corrosion resistance in coated systems. Conversely, samples with more negative E_{corr} values, such as (Mn,Co,Cd,Cu,Zn)Fe_2O_4-T15 (≈ −0.21 V), exhibit the lowest i_{corr} values, demonstrating that corrosion rate is more strongly governed by charge transfer kinetics, coating permeability, and microstructural features than by E_{corr} alone [85].

3.6. Electrochemical Impedance Behavior of EPD Coatings

Electrochemical impedance spectroscopy (EIS) was employed to evaluate the corrosion protection performance of the coatings by analyzing the real and imaginary impedance components under AC perturbation. The Nyquist plots (Fig.12), along with Bode modulus and phase angle diagrams (Fig.13 and Fig.14), obtained after 2 h immersion in 3.5 wt.% NaCl at room temperature, represent the near steady-state response of the system, minimizing transient effects associated with initial electrolyte penetration [86].

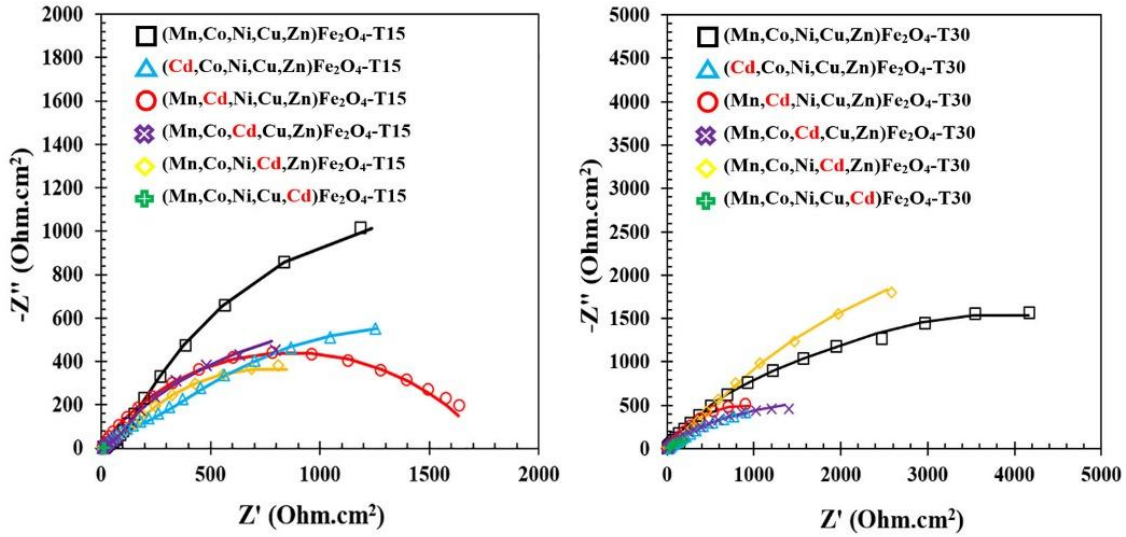

Fig. 12. Nyquist diagram of coated samples with two polymerization times of 15 and 30 hours

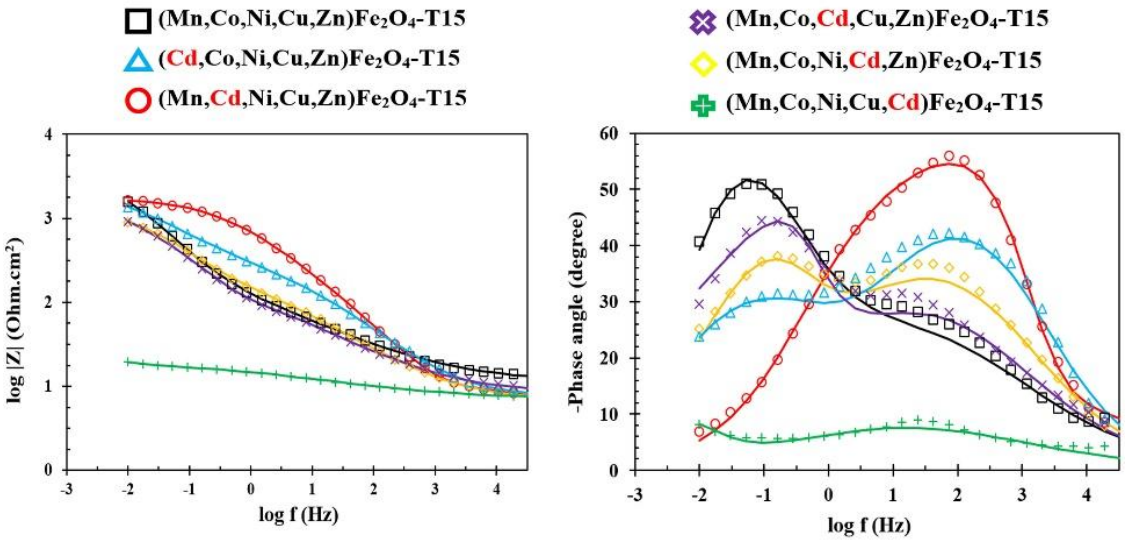

Fig. 13. Bode and Bode-phase diagrams of coated samples with 15 hour polymerization time

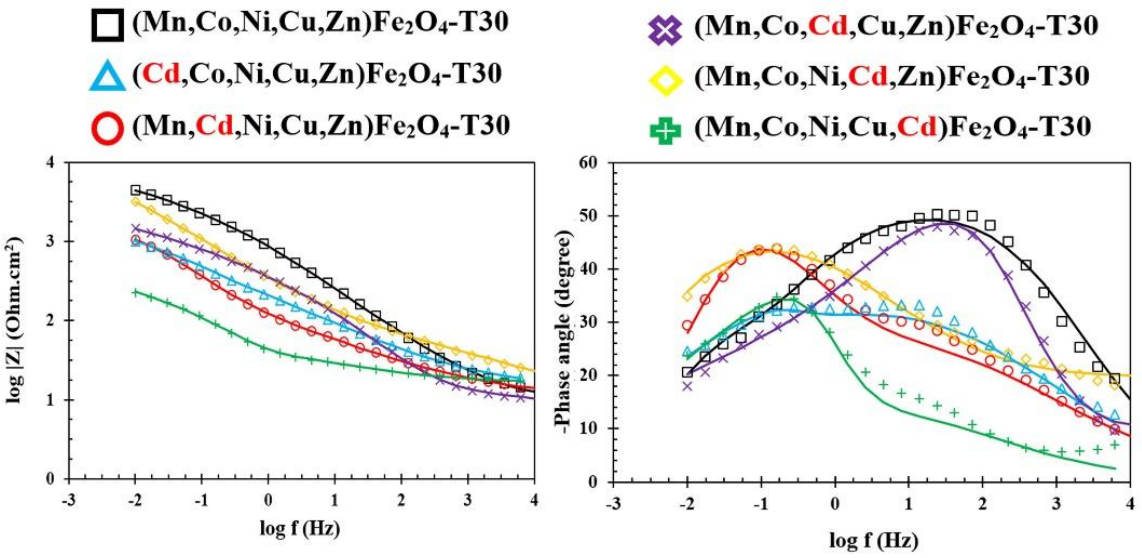

Fig. 14. Bode and Bode-phase diagrams of coated samples with 30 hour polymerization time

The presence of two distinct time constants in all samples, confirmed by Bode phase plots, indicates a permeable coating layer and an active metal/electrolyte interface. Accordingly, the impedance data were fitted using a two-time-constant equivalent circuit (Fig.15), consisting of solution resistance (R_s), coating resistance (R_c), charge transfer resistance (R_{ct}), and two constant phase elements (CPE_c and CPE_{dl}). The use of constant phase elements instead of ideal capacitors accounts for surface roughness, heterogeneity, and non-uniform current distribution [87]. The good agreement between experimental and simulated data using ZsimpWin confirms the validity of the selected equivalent circuit model.

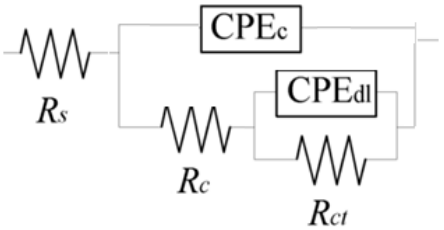

Fig. 15. Electrochemical equivalent circuit model featuring two time constants used for fitting EIS data

The values of the different elements of the electrochemical equivalent circuit are presented in Table 4. The solution resistance (R_s) remains within a narrow range (≈6–16 Ω·cm²), indicating similar electrolyte conditions for all tests and a negligible contribution to corrosion differences. Therefore, the analysis focuses on R_c, R_{ct}, and related parameters. Coating resistance (R_c), which reflects the barrier property against electrolyte penetration, varies significantly with composition and polymerization time. Low R_c values in some 15 h samples, such as (Mn,Cd,Ni,Cu,Zn)Fe_2O_4-T15 (≈6 Ω·cm²), indicate high permeability and the presence of effective diffusion paths. In contrast, a substantial increase in R_c (up to ≈3489 Ω·cm²) is observed for (Mn,Co,Ni,Cu,Zn) Fe_2O_4-T30, attributed to enhanced polymer crosslinking and reduced PEI solubility.

Table 4
Characteristics of the equivalent circuit elements simulated from the EIS test

Sample Name	R_s (ohm.cm²)	Y_{0c} (mS.sec^n .cm^{-2})	n_1	R_c (ohm.cm²)	Y_{0dl} (mS.sec^n .cm^{-2})	n_2	R_{ct} (ohm.cm²)	R_t (ohm.cm²)
(Mn,Co,Ni,Cu,Zn)Fe_2O_4(T15)	12.09	1.99	0.57	89.65	3.85	0.75	3235	3324.65
(Mn,Co,Ni,Cu,Zn)Fe_2O_4 (T30)	9.76	0.32	0.60	3489	1.36	0.69	3203	6692
(Cd,Co,Ni,Cu,Zn)Fe_2O_4 (T15)	7.40	0.43	0.60	281.5	1.94	0.52	2400	2681.5
(Cd,Co,Ni,Cu,Zn)Fe_2O_4 (T30)	13.63	2.07	0.50	1391	0.96	0.99	1078	2469
(Mn,Cd,Ni,Cu,Zn)Fe_2O_4(T15)	6.14	0.34	0.57	6.31	0.01	0.95	1762	1768.31
(Mn,Cd,Ni,Cu,Zn)Fe_2O_4 (T30)	11.55	2.84	0.52	91.39	4.22	0.71	1577	1668.39
(Mn,Co,Cd,Cu,Zn)Fe_2O_4(T15)	8.24	2.68	0.54	201.1	1.35	0.93	2911	3112.1
(Mn,Co,Cd,Cu,Zn)Fe_2O_4(T30)	16.04	1.11	0.52	12.6	0.18	0.78	4055	4067.6
(Mn,Co,Ni,Cd,Zn)Fe_2O_4(T15)	6.75	1.54	0.51	246.8	2.04	0.76	1263	1509.8
(Mn,Co,Ni,Cd,Zn)Fe_2O_4 (T30)	8.36	2.71	0.58	338.6	1.39	0.63	7205	7543.6
(Mn,Co,Ni,Cu,Cd)Fe_2O_4 (T15)	6.99	29.54	0.52	12.75	3.76	0.97	5.74	18.49
(Mn,Co,Ni,Cu,Cd)Fe_2O_4 (T30)	16.34	8.99	0.53	40.69	3.71	0.94	462.6	503.29

However, increased R_c does not necessarily correspond to improved corrosion resistance, as longer polymerization also leads to larger and more connected cracks. This dual behavior results in discrepancies between R_c and R_{ct} values. Charge transfer resistance (R_{ct}), directly related to corrosion kinetics, provides a more reliable indicator of corrosion resistance. High R_{ct} values, such as ≈7205 Ω·cm² for (Mn,Co,Ni,Cd,Zn) Fe_2O_4-T30, indicate effective suppression of electrochemical reactions, likely due to favorable composition and stable passive film formation. Conversely, very low Rct values, such as ≈5.74 Ω·cm² for (Mn,Co,Ni,Cu,Cd) Fe_2O_4-T15, reflect active corrosion and poor protective performance, consistent with a highly cracked microstructure [52].

The parameters of the coating constant phase element (CPE_c), particularly the exponent n_1 (≈0.5–0.6), indicate significant deviation from ideal capacitive behavior, reflecting surface roughness, structural heterogeneity, and non-uniform crack distribution [88, 89]. Higher admittance values (Y_{0c}) are associated with increased effective capacitance and higher electrolyte permeability [90], whereas lower values suggest a denser and less permeable coating [91]. Similarly, the double-layer constant phase element (CPE_{dl}) and exponent n_2 provide insight into the metal/electrolyte interface. Values of n_2 close to unity, such as 0.99 for (Cd,Co,Ni,Cu,Zn)Fe_2O_4-T30, indicate near-ideal capacitive behavior and a more uniform passive layer, whereas lower values suggest interfacial heterogeneity and localized corrosion activity.

The total resistance ($R_t = R_c + R_{ct}$) is used as an overall indicator of corrosion resistance. The results show that coatings with an optimal balance between barrier properties and charge transfer inhibition exhibit the highest R_t values (Fig.16). For example, (Mn,Co,Ni,Cd,Zn)Fe_2O_4-T30 shows the highest R_t (≈7544 Ω·cm²), indicating superior protective performance under near steady-state conditions.

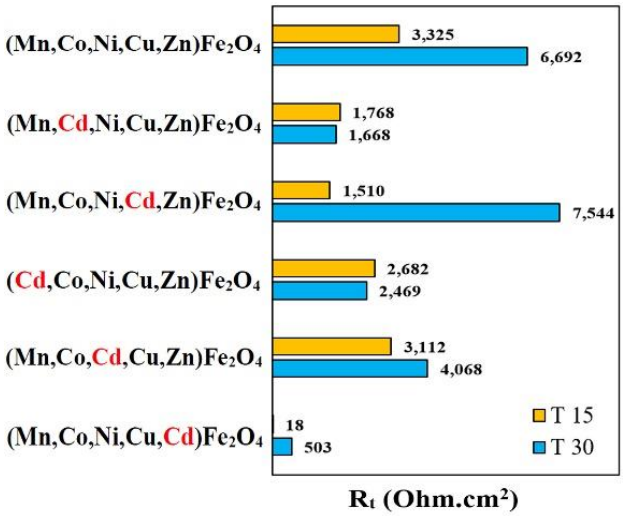

Fig. 16. Total resistance plots of the samples coated with polymerization times of 15 hours (T15) and 30 hours (T30)

The effect of polymerization time is composition-dependent. In some cases, increasing the time from 15 to 30 h enhances Rt due to improved polymer crosslinking, reduced solubility, and better adhesion. However, in other cases, increased crack size and connectivity dominate, leading to reduced R_t. This highlights the need for a balance between chemical integrity and microstructural control in optimizing coating performance.

5. CONCLUSION

High-entropy spinel ferrite/PEI composite coatings were successfully deposited on copper substrates using electrophoretic deposition under optimized conditions (200 V, 3 min, 2 g/L SDS), which produced uniform and adherent coatings. The deposition mechanism was governed by a multi-component system, where zeta potential shifted from near-neutral values (+1.57 to −0.94 mV) to more negative values (−6.81 to −10.46 mV), confirming enhanced electrophoretic mobility due to SDS and the formation of PEI–Cu^{2+} complexes generated by the active copper anode.

Microstructural analysis showed that increasing polymerization time from 15 to 30 h improved coating adhesion and cohesion but significantly increased crack size. Crack severity followed the order (Mn,Co,Ni,Cu,Zn)Fe_2O_4 < (Mn,Cd,Ni,Cu,Zn) Fe_2O_4 < (Mn,Co,Cd,Cu,Zn) Fe_2O_4 < (Mn,Co,Ni,Cd,Zn) Fe_2O_4 < (Cd,Co,Ni,Cu,Zn) Fe_2O_4 < (Mn,Co,Ni,Cu,Cd) Fe_2O_4, demonstrating the strong influence of Cd on stress concentration and crack propagation.

All coatings retained ferromagnetic behavior, although magnetic parameters decreased compared to powders due to polymer-induced dilution, reduced exchange interactions, and the presence of ~5 at.% diamagnetic Cu.

Electrochemical measurements showed that Cd incorporation reduced corrosion current density from 2.15 μA/cm² for Cd-free coatings to 0.1–1.12 μA/cm² in most Cd-containing samples (e.g., 0.1 μA/cm² for (Mn,Co,Cd,Cu,Zn) Fe_2O_4-T15). However, increasing polymerization time could increase icorr (e.g., from 0.1 to 5 μA/cm²), indicating the dominant effect of crack growth.

EIS analysis revealed that corrosion resistance is controlled by the balance between coating resistance (R_c) and charge transfer resistance (R_{ct}). The highest performance was observed for (Mn,Co,Ni,Cd,Zn)Fe_2O_4-T30, with R_{ct} ≈ 7205 Ω·cm² and total resistance R_t ≈ 7544 Ω·cm², whereas poor performance was associated with low Rct values (e.g., ≈5.74 Ω·cm² for (Mn,Co,Ni,Cu,Cd)Fe_2O_4-T15).

Overall, the results demonstrate that coating performance is quantitatively governed by the interplay between composition, polymerization time, and microstructure, and that optimal corrosion resistance is achieved only when improved adhesion is balanced with controlled crack formation.

Acknowledgements

We express our gratitude to the University of Sistan and Baluchestan for generously providing the necessary laboratory facilities for the successful execution of this research. Additionally, our sincere thanks go to Fereydoun Oukati Sadeq and Mahdi Shafiee Afarani for their invaluable assistance.

REFERENCES

[1] Yang Z, Xiang X, Yang J, Zhao ZY. High-entropy oxides as energy materials: from complexity to rational design. Mater Futures. 2024;3(4):042103.

[2] Nechvoglod O, Ostovari Moghaddam A, Pratskova S, Trofimova S, Samodurova M, Trofimov E. A review on high-entropy alloys coatings fabricated by electrodeposition: the correlation between composition, properties and processing parameters. JOM. 2025;77(3):1005–1028.

[3] Sun Y, Dai S. High-entropy materials for catalysis: a new frontier. Sci Adv. 2021;7(20):eabg1600.

[4] Tomboc GM, Zhang X, Choi S, Kim D, Lee LYS, Lee K. Stabilization, characterization, and electrochemical applications of high-entropy oxides: critical assessment of crystal phase–properties relationship. Adv Funct Mater. 2022;32(43):2205142.

[5] Fracchia M, Coduri M, Ghigna P, Anselmi-Tamburini U. Phase stability of high entropy oxides: a critical review. J Eur Ceram Soc. 2024;44(2):585–594.

[6] Mohafez FS, Davarpanah AM, Rahdar A, Beyzaei H, Zeybek O, Barrett S. Structural, magnetic, and in vitro inhibitory characteristics of Ce-substituted MnFe2O4 nanoparticles. Appl Phys A. 2021;127(8):600.

[7] Davarpanah AM, Rahdar A, Dastnae MA, Zeybek O, Beyzaei H. (1−x)BaFe12O19/xCoFe2O4 hard/soft

magnetic nanocomposites: synthesis, physical characterization, and antibacterial activities study. J Mol Struct. 2019;1175:445–449.
[8] Rahdar S, Rahdar A, Sattari M, Hafshejani LD, Tolkou AK, Kyzas GZ. Barium/cobalt@polyethylene glycol nanocomposites for dye removal from aqueous solutions. Polymers. 2021;13(7):1161.
[9] Rahmani E, Shamsabadipour A, Ahmadi M, Rahdar A, Díez Pascual AM. Role of iron oxide (Fe2O3) nanocomposites in advanced biomedical applications: a state-of-the-art review. 2022.
[10] Ai J, et al. Microstructural evolution and catalytic properties of novel high-entropy spinel ferrites MFe2O4 (M=Mg, Co, Ni, Cu, Zn). Ceram Int. 2023;49(14):22941–22951.
[11] Wei C, et al. Valence change ability and geometrical occupation of substitution cations determine the pseudocapacitance of spinel ferrite XFe2O4 (X=Mn, Co, Ni, Fe). Chem Mater. 2016;28(12):4129–4133.
[12] Ma J, et al. High-entropy spinel ferrites MFe2O4 (M=Mg, Mn, Fe, Co, Ni, Cu, Zn) with tunable electromagnetic properties and strong microwave absorption. J Adv Ceram. 2022;11(5):754–768.
[13] Liu X, et al. Insight of multi-polarization effect by constructing high-entropy spinel ferrite/perovskite@amorphous carbon for enhancing electromagnetic wave absorption. Chem Eng J. 2025;516:164053.
[14] Liu X, Tian F, Sheng J, Yu Y, Yang W. High-entropy porous spinel ferrite@amorphous carbon nanocomposites with abundant structural defects for wide-band electromagnetic wave absorption. Chem Eng J. 2024;490:151848.
[15] Ma J, Liu T, Ye W, He Q, Chen K. High-entropy perovskite oxides for energy materials: a review. J Energy Storage. 2024;90:111890.
[16] Ghamkhari A, Mohamadi L, Kazemzadeh S, Zafar MN, Rahdar A, Khaksefidi R. Synthesis and characterization of poly(styrene-block-acrylic acid) diblock copolymer modified magnetite nanocomposite for efficient removal of penicillin G. Compos Part B Eng. 2020;182:107643.
[17] Pourmadadi M, et al. Role of iron oxide (Fe2O3) nanocomposites in advanced biomedical applications: a state-of-the-art review. Nanomaterials. 2022;12(21):3873.
[18] Rahdar S, Rahdar A, Sattari M, Hafshejani LD, Tolkou AK, Kyzas GZ. Barium/cobalt@polyethylene glycol nanocomposites for dye removal from aqueous solutions. Polymers. 2021;13(7).
[19] Sarkar A, et al. High entropy oxides for reversible energy storage. Nat Commun. 2018;9(1):3400.
[20] Goodenough J, Loeb A. Theory of ionic ordering, crystal distortion, and magnetic exchange due to covalent forces in spinels. Phys Rev. 1955;98(2):391.
[21] Chang X, et al. High-entropy spinel ferrites with broadband wave absorption synthesized by simple solid-phase reaction. Molecules. 2023;28(8):3468.
[22] Han L, et al. Multifunctional high-entropy materials. Nat Rev Mater. 2024;9(12):846–865.
[23] Sharma N. Ferrite nanoparticles for corrosion protection applications. In: Engineered ferrites and their applications. Springer; 2023. p. 227–240.
[24] Gharagozlou M, Ramezanzadeh B, Baradaran Z. Synthesis and characterization of a novel anticorrosive cobalt ferrite nanoparticles dispersed in silica matrix (CoFe2O4–SiO2) to improve corrosion protection performance of epoxy coating. Appl Surf Sci. 2016;377:86–98.
[25] Boris I, Kharisova H, Dias VR, Oxana B, Kharissova V. Mini-review: ferrite nanoparticles in catalysis. Arab J Chem. 2019;212:1234–1246.
[26] Kaya C, Kaya F, Atiq S, Boccaccini A. Electrophoretic deposition of ceramic coatings on ceramic composite substrates. Br Ceram Trans. 2003;102(3):99–102.
[27] Ammam M. Electrophoretic deposition under modulated electric fields: a review. RSC Adv. 2012;2(20):7633–7646.
[28] Sarkar P, Nicholson PS. Electrophoretic deposition (EPD): mechanisms, kinetics, and application to ceramics. J Am Ceram Soc. 1996;79(8):1987–2002.
[29] Karimian H, Baba LA. Effect of polymeric binder and dispersant on the stability of colloidal alumina suspensions. 2006.
[30] Khosravi M, Sharafi S, Irannejad A. Investigating the effect of Cd on the structure and magnetic properties of (Mn, Co, Ni, Cu, Zn)Fe2O4 high entropy spinel oxide. Appl Phys A. 2024;130(5):335.
[31] Navarro RR, Wada S, Tatsumi K. Heavy metal precipitation by polycation–polyanion complex of PEI and its phosphonomethylated derivative. J Hazard Mater. 2005;123(1–3):203–209.
[32] Chen M, Hankins NP. Interaction among branched polyethylenimine (PEI), sodium dodecyl sulfate (SDS) and metal cations during copper recovery from water using polymer–surfactant aggregates. J Water Process Eng. 2020;34:101170.
[33] Mészáros R, Thompson L, Bos M, Varga I, Gilányi T. Interaction of sodium dodecyl sulfate with polyethyleneimine: surfactant-induced polymer solution colloid dispersion transition. Langmuir. 2003;19(3):609–615.
[34] Mamardashvili G, Kaigorodova EY, Khodov I, Mamardashvili N. Interaction of cationic 5,10,15,20-tetra(N-methylpyridyl) porphyrin and its Co(III) complex with premicellar SDS aggregates: structure and properties. J Mol Liq. 2024;400:124549.
[35] Sa'adati H, Raissi B, Riahifar R, Yaghmaee MS. How preparation of suspensions affects the electrophoretic deposition phenomenon. J Eur Ceram Soc. 2016;36(2):299–305.
[36] Ustyakina D, Chevtaev A, Tabunshchikov A, Ozerin A, Radchenko F, Novakov I. Complexes of polyethyleneimine with Cu^{2+} ions in aqueous solutions as precursors for obtaining copper nanoparticles. Polym Sci Ser B. 2019;61(3):261–265.
[37] Sultana S, Khan MZ, Umar K. Synthesis and characterization of copper ferrite nanoparticles doped polyaniline. J Alloys Compd. 2012;535:44–49.

[38] Goon IY, Zhang C, Lim M, Gooding JJ, Amal R. Controlled fabrication of polyethylenimine-functionalized magnetic nanoparticles for the sequestration and quantification of free Cu^{2+}. Langmuir. 2010;26(14):12247–12252.
[39] Shati AA, et al. Functionalization of porous silica with graphene oxide and polyethyleneimine containing zinc copper ferrite nanoparticles for water treatment and antibacterial application. Environ Pollut. 2024;348:123745.
[40] Ozerin A, Kurkin T, Radchenko F, Shulevich YV, Novakov I. Complexes of polyethyleneimine with copper and cobalt ions as precursors for preparing metal nanoparticles. Russ J Appl Chem. 2021;94(2):210–216.
[41] Besra L, Liu M. A review on fundamentals and applications of electrophoretic deposition (EPD). Prog Mater Sci. 2007;52(1):1–61.
[42] Mohammadi MM, Vossoughi M, Feilizadeh M, Rashtchian D, Moradi S, Alemzadeh I. Effects of electrophoretic deposition parameters on the photocatalytic activity of TiO2 films: optimization by response surface methodology. Colloids Surf A. 2014;452:1–8.
[43] Wang YC, Leu IC, Hon MH. Kinetics of electrophoretic deposition for nanocrystalline zinc oxide coatings. J Am Ceram Soc. 2004;87(1):84–88.
[44] Tang X, Li R, Han D, Wu X. Impacts of electrokinetic isolation of phosphorus through pore water drainage on sediment phosphorus storage dynamics. Environ Pollut. 2020;266:115210.
[45] Elansezhian R, Ramamoorthy B, Nair PK. Influence of SDS and CTAB surfactants on the surface morphology and topography of electroless Ni–P deposits. J Mater Process Technol. 2009;209(1):233–240.
[46] Michaelis E, Wöhrle D, Rathousky J, Wark M. Electrodeposition of porous zinc oxide electrodes in the presence of sodium lauryl sulfate. Thin Solid Films. 2006;497(1–2):163–169.
[47] Aishwarya V, Suganthi K, Rajan K. Transport properties of nano manganese ferrite–propylene glycol dispersion (nanofluids): new observations and discussion. J Nanopart Res. 2013;15(7):1774.
[48] Plaza R, De Vicente J, Gomez-Lopera S, Delgado A. Stability of dispersions of colloidal nickel ferrite spheres. J Colloid Interface Sci. 2001;242(2):306–313.
[49] Zhu L, Han Y, Tian M, Wang Y. Complex formation and aggregate transitions of sodium dodecyl sulfate with an oligomeric connecting molecule in aqueous solution. Langmuir. 2013;29(39):12084–12092.
[50] Van Tassel JJ, Randall CA. Mechanisms of electrophoretic deposition. Key Eng Mater. 2006;314:167–174.
[51] Nolis GM, et al. Electrochemical reduction of a spinel-type manganese oxide cathode in aqueous electrolytes with Ca^{2+} or Zn^{2+}. J Phys Chem C. 2018;122(8):4182–4188.
[52] Wang HL, Dai JG, Sun XY, Zhang XL. Characteristics of concrete cracks and their influence on chloride penetration. Constr Build Mater. 2016;107:216–225.
[53] Neu M, Sitterberg J, Bakowsky U, Kissel T. Stabilized nanocarriers for plasmids based upon cross-linked poly(ethylene imine). Biomacromolecules. 2006;7(12):3428–3438.
[54] Jeon S, Min J, Kim SH, Lee KB. Introduction of cross-linking agents to enhance the performance and chemical stability of polyethyleneimine-impregnated CO2 adsorbents: effect of different alkyl chain lengths. Chem Eng J. 2020;398:125531.
[55] Al Sunbul H, Silikas N, Watts DC. Polymerization shrinkage kinetics and shrinkage-stress in dental resin-composites. Dent Mater. 2016;32(8):998–1006.
[56] Huang YJ, Liang CM. Volume shrinkage characteristics in the cure of low-shrink unsaturated polyester resins. Polymer. 1996;37(3):401–412.
[57] Lugovy M, Slyunyayev V, Teixeira V. Residual stress relaxation processes in thermal barrier coatings under tension at high temperature. Surf Coat Technol. 2004;184(2–3):331–337.
[58] Meng F, David J, Bollin S, Nichols M, Thouless M. Kinetics of channeling cracks in polymeric coatings. Int J Solids Struct. 2018;132:105–113.
[59] Ge J, Turunen M, Kusevic M, Kivilahti J. Effects of surface treatment on the adhesion of copper to a hybrid polymer material. J Mater Res. 2003;18(11):2697–2707.
[60] Kisin S, Van der Varst PT, De With G. Adhesion and adhesion changes at the copper metal–(acrylonitrile–butadiene–styrene) polymer interface. Thin Solid Films. 2007;515(17):6853–6859.
[61] Hao L, et al. Hydrothermal engineering of triple-scale corrosion resistance: structural barrier, oxygen vacancy, and surface functionalization in Ce–NiCo-LDH coatings. J Colloid Interface Sci. 2025:137981.
[62] Tomasino E. Experimental and theoretical strategies for a rational design of polyamine-based anion exchange membranes. 2025.
[63] Wanjari SS, Nandanwar DV, Rewatkar K, Gongal AV. Investigating impact of Ni–Cd substitution on structural, magnetic and optical properties of nanosize Al ferrites. Heliyon. 2024;10(21).
[64] Verma K, Sharma S. Influence of addition of copper cadmium ferrite on the dielectric and electrical behavior of BaSrTiO3 ceramics. Ceram Int. 2012;38(7):5957–5966.
[65] Reitz C, Suchomski C, Chakravadhanula VSK, Djerdj I, Jagličić Z, Brezesinski T. Morphology, microstructure, and magnetic properties of ordered large-pore mesoporous cadmium ferrite thin film spin glasses. Inorg Chem. 2013;52(7):3744–3754.
[66] Resta IM, Horwitz G, Elizalde MLM, Jorge GA, Molina FV, Antonel PS. Magnetic and conducting properties of composites of conducting polymers and ferrite nanoparticles. IEEE Trans Magn. 2013;49(8):4598–4601.

[67] Hamciuc C, Asandulesa M, Hamciuc E, Roman T, Olariu MA, Pui A. Novel polyimide/copper-nickel ferrite composites with tunable magnetic and dielectric properties. Polymers. 2021;13(10):1646.
[68] Stabik J, Dybowska A, Pluszyński J, Szczepanik M, Suchoń Ł. Magnetic induction of polymer composites filled with ferrite powders. Arch Mater Sci Eng. 2010;41(1):13–20.
[69] Ning S, Wang S, Liu Z, Zhang N, Yang B, Zhang F. Study on magnetic and plasmonic properties of Fe3O4-PEI-Au and Fe3O4-PEI-Ag nanoparticles. Materials. 2024;17(2):509.
[70] Aslibeiki B, et al. Magnetic hyperthermia properties of CoFe2O4 nanoparticles: effect of polymer coating and interparticle interactions. Ceram Int. 2022;48(19):27995–28005.
[71] Abdolrahimi M, et al. Magnetism of nanoparticles: effect of the organic coating. Nanomaterials. 2021;11(7):1787.
[72] Chaturvedi S, Shirolkar MM, Rajendra R, Singh S, Ballav N, Kulkarni S. Coercivity and exchange bias of bismuth ferrite nanoparticles isolated by polymer coating. J Appl Phys. 2014;115(12).
[73] El-Bassuony AAH, Gamal WM, Abdelsalam HK. Study of adding nanocomposite cobalt nano ferrite to silver nanoparticles with magnetite impurity. J Mater Sci Mater Electron. 2022;33(20):16219–16235.
[74] Karadimov TR, Nenova EP, Pavlova EL, Ivanova IA, Georgieva MT, Georgiev PA. Structure, ecotoxicity, redox and bactericidal activity of Cu-containing nanocrystalline ferrites. Molecules. 2025;30(22).
[75] Araújo EV, et al. Tunable dielectric and microwave properties of epoxy composites with CoFe2O4 and MgFe2O4 spinel ferrites. Appl Phys A. 2025;131(9):708.
[76] Mazurenko R, et al. Synthesis of nanosized spinel ferrites MnFe2O4 on the surface of carbon nanotubes for polymer composites with enhanced microwave absorption. Appl Mater Today. 2023;35:101972.
[77] Fulco APP, Melo JDD, Paskocimas CA, Medeiros SN, Machado FLA, Rodrigues AR. Magnetic properties of polymer matrix composites with embedded ferrite particles. NDT E Int. 2016;77:42–48.
[78] Hu Z, et al. Characterization of ferrite magnetic nanoparticle modified polymeric composites by modeling. J Magn Magn Mater. 2020;493:165735.
[79] Rodič P, Milošev I. Corrosion inhibition of pure aluminium and alloys AA2024-T3 and AA7075-T6 by cerium(III) and cerium(IV) salts. J Electrochem Soc. 2016;163(3):C85.
[80] Lata A, Mandal N. Investigation of the effect of electrode distance on the polarization impedance type flowmeter. IEEE Sens J. 2019;19(15):6279–6288.
[81] MacDonald JR. Theory of space-charge polarization and electrode-discharge effects. J Chem Phys. 1973;58(11):4982–5001.
[82] Adhikari A, Claesson P, Pan J, Leygraf C, Dédinaité A, Blomberg E. Electrochemical behavior and anticorrosion properties of modified polyaniline dispersed in polyvinylacetate coating on carbon steel. Electrochim Acta. 2008;53(12):4239–4247.
[83] Trentin A, Pakseresht A, Duran A, Castro Y, Galusek D. Electrochemical characterization of polymeric coatings for corrosion protection: a review of advances and perspectives. Polymers. 2022;14(12):2306.
[84] Piletska EV, Guerreiro AR, Whitcombe MJ, Piletsky SA. Influence of the polymerization conditions on the performance of molecularly imprinted polymers. Macromolecules. 2009;42(14):4921–4928.
[85] Esmailzadeh S, Aliofkhazraei M, Sarlak H. Interpretation of cyclic potentiodynamic polarization test results for corrosion behavior of metals: a review. Prot Met Phys Chem Surf. 2018;54(5):976–989.
[86] Olivier MG, Poelman M. Use of electrochemical impedance spectroscopy (EIS) for the evaluation of electrocoatings performances. London: InTech; 2012.
[87] Lasia A. Electrochemical impedance spectroscopy and its applications. In: Modern aspects of electrochemistry. Springer; 2002. p. 143–248.
[88] Bouvet G, Nguyen DD, Mallarino S, Touzain S. Analysis of the non-ideal capacitive behaviour for high impedance organic coatings. Prog Org Coat. 2014;77(12):2045–2053.
[89] Farooq SA, Raina A, Mohan S, Singh RA, Jayalakshmi S, Ul Haq MI. Nanostructured coatings: review on processing techniques, corrosion behaviour and tribological performance. Nanomaterials. 2022;12(8):1323.
[90] Liu XH, Kou LQ, Shi T, Liu K, Chen L. High rate capability and high voltage cycling stability of Y2O3-coated LiNi0.5Co0.2Mn0.3O2. J Power Sources. 2014;267:874–880.
[91] Wu X, et al. Electrolyte permeation and ion diffusion enhanced architectures for high performance all-solid-state flexible supercapacitors. J Power Sources. 2021;482:228996.